

A Multi-DOF Self-Moving Piezoelectric Actuator With High Carrying/Positioning Capability by Constructing a Multi-Vibration-Tailored Non-uniformly Distributed Electrode

Jinshuo Liu , Zhaochun Ding , Zihan Zhu , Jiang Wu , Xuewen Rong , Rui Song , and Yibin Li 

Abstract—This article presents a multi-DOF self-moving piezoelectric actuator (MDSMPA) by constructing a multivibration-tailored nonuniformly distributed electrode. Here, the fourth-order bending (B_4) and third-order bending (B_3) vibrations are excited to generate the translational and rotational movements, respectively, inspired by the kangaroo's walking and rotating gaits in terms of the driving feet's alternating movement pattern and the tail's supporting function. Initially, the ring-shaped electrode was divided nonuniformly to balance the electromechanical coupling properties of the B_3 and B_4 vibrations. Subsequently, the feet's positions were decided to efficiently generate multi-DOF movements. Finally, a prototype with the size of $\Phi 50 \times 7.5 \text{ mm}^3$ and the weight of 32.8 g was fabricated to assess its performance. At 36.4 and 20.6 kHz, the MDSMPA yielded the maximal translational and rotational speeds of 138.2 mm/s and 23.5 rad/s, respectively. It carried the maximal payload of 5130 g (equal to 156.4 times its weight), crossed the 11-mm-wide gully, and climbed the 10.1° slope. Moreover, by employing an onboard circuit with controlling, driving, and insulating functions, the MDSMPA accomplished the untethered movements, where the minimal stepwise displacement and stepwise angle reached 117 nm and 2.4 μrad , respectively, and performed the inspection in a narrow tube.

Index Terms—Multi-DOFs, nonuniformly distributed electrode, ultrasonic actuation, untethered self-moving piezoelectric actuator.

Received 24 January 2025; revised 2 May 2025; accepted 27 June 2025. Recommended by Technical Editor P. Pathak and Senior Editor C. Clévy. This work was supported in part by the National Natural Science Foundation of China (NSFC) under Grant 52475022 and Grant 52105029, in part by the Science Center Program of NSFC under Grant 62188101, and in part by Foundation of Taishan Scholar Project under Grant tsqn202306052. (Corresponding author: Jiang Wu.)

Jinshuo Liu, Zhaochun Ding, Jiang Wu, Xuewen Rong, Rui Song, and Yibin Li are with the School of Control Science and Engineering, Shandong University, Jinan 250061, China (e-mail: liujinshuo@mail.sdu.edu.cn; dingzhaochun@mail.sdu.edu.cn; wujiang@sdu.edu.cn; rongxw@sdu.edu.cn; rsong@sdu.edu.cn; liyb@sdu.edu.cn).

Zihan Zhu is with the School of Electrical and Automation Engineering, Shandong University of Science and Technology, Qingdao 266590, China (e-mail: zhuzihan@sdu.edu.cn).

This article has supplementary material provided by the authors and color versions of one or more figures available at <https://doi.org/10.1109/TMECH.2025.3585598>.

Digital Object Identifier 10.1109/TMECH.2025.3585598

I. INTRODUCTION

PIEZOELECTRIC actuators (PAs) offer simple structure [1], [2], absence of electromagnetic (EM) interference [3], [4], and self-locking at the power-OFF state [5], [6]; compared to EM motors. In recent years, PAs have been applied to optical devices [7], [8], miniature robots [9], [10], and medical instruments [11], [12]. To promote the extensive and in-depth application, it is essential to develop the PAs with multi-DOFs and high carrying/positioning capability. In specific, first, multi-DOFs of the PAs contribute to improving the miniature robots' adaptability to complicated environments, e.g., tube inspection [13], [14]. Second, increasing usage of functional components (e.g., lenses, circuits, or injectors) necessitates high carrying capability (indicated as the payload-to-weight ratio) [15], [16]. Third, the small stepwise displacement is required for precise manipulation (e.g., light path's adjustment or defect detection of wafer surface) [17], [18].

In general, the PAs operate by the principles of direct-driving, stick-slip, inchworm, and resonant-actuating [19], [20]. The direct-driving PAs typically utilize the direct extension of the piezoelectric stacks to produce the force/displacement, which brings nanometer resolution but limited stroke [18]. For instance, Li and Xu [17] used two decoupled prismatic limbs to establish a positioning stage, which produced 220 nm resolution, but the workspace was only $132 \times 126 \mu\text{m}^2$. Wang et al.'s [21] parallel positioning stage had two DOFs but $1.4 \times 1.2 \text{ mm}^2$ workspace. Basically, the stick-slip PAs are driven by alternately generating the slow-extending and quick-retracting motions [22], [23]. As typical examples, Li et al.'s [19] L-shaped actuator had 84 nm resolution and 1100 g payload. Inspired by the forefoot of the mantis, Yan et al. [20] designed a PA that has the resolution and speed of 0.33 μrad and 4.5 rad/s, respectively. However, the backward motion inevitably exists during the slip state, which reduces the positioning capability [24], [25]. The inchworm PAs accumulate the single-step displacement induced by the piezoelectric stacks [26]. Deng et al. [27] used the three-jaw-type clamping mechanism and six piezoelectric stacks to devise a cylindrical inchworm actuator with 12.3 N thrust force. Despite large output force, the inchworm PAs are complex in control strategy and/or structure [28], [29]. The resonant-actuating PAs operate in the resonant states to drive the sliders or rotors [30],

[31]. Owing to the high output force and the input signal's adjustability [32], they exhibit the potential to achieve high carrying/positioning capability.

The resonant-actuating PAs are divided into the traveling-wave PAs (TWPAs) and the standing-wave PAs (SWPAs) [33]. The TWPAs utilize the superposition of resonant vibrations to generate the traveling wave, which allows the foot to move in an elliptical trajectory [34]. Hariri et al. [35] designed a plate-shaped TWPA with three DOFs and the maximal payload of 90 g. Wang et al. [36] devised a millipede-inspired TWPA with one DOF and the maximal payload of 433 g. Despite stable operation, the TWPAs suffer from the intensive energy loss due to the wave reflection at the boundaries as well as the difficulty in miniaturization owing to the fact that their lengths should be sufficient for superpositioning the vibrations [37]. While, such spatial requirement does not exist for the SWPAs, so their configurations can be flexibly designed to a larger extent [6]. Baisch et al.'s [38] micro actuator provided the one-DOF translational movement with 1.35 g payload. Dharmawan et al.'s [39] one-DOF actuator, though which weighted 3 g, carried the maximal payload of 100 g. The SWPAs usually adopt the rectangular configurations, most of whose vibration modes allow the SWPAs to provide the translational self-movement(s) [37]. However, the rectangular structure's nonrotational symmetry [40] results in its absence of the rotational vibration modes, which makes it difficult to generate the rotation and consequently limits the SWPAs' DOFs [41]. On the other hand, irregular structure is an approach to guarantee multi-DOFs particularly for the SWPAs. Zhao et al. [42] devised a three-DOF actuator with monopod structure by exciting the elliptical trajectory on each foot, but the usage of five feet resulted in large volume/weight. Li et al.'s actuator [43] achieved the multi-DOF movement by utilizing two piezo-legs, where the vibrations should be intensively excited with the extremely thin beams. Intrinsically, irregular structure enriches the types of the vibration modes and facilitates the realization of multi-DOFs [33], but its fabricating difficulty and the high expense restrict these SWPAs' application.

In terms of simple structure and rotational symmetry [37], the ring shape is a candidate configuration for the SWPAs. As a typical example, Li et al.'s actuator [44] adopted the ring shape to achieve the three-DOF movement, but its maximal payload corresponding to the rotational movement (>200 g) was over that to the translational movement. Since the lead-zirconate-titanate (PZT) plates are uniformly arranged on the vibrating body, the area for exciting a certain vibration mode cannot well match the region capable of efficiently generating another mode, so strong electromechanical couplings are not easy to achieve for all vibration modes necessary for generating the translational and rotational movements.

Vibration-tailored nonuniform distribution of the electrode would be an approach to tackle this problem. In specific, when certain portion(s) of the electrode overlaps the efficiently exciting region shared by two (or more) vibration modes, by switching the frequency, the electromechanical coupling properties can be balanced among the vibration modes. Meanwhile, this approach does not increase the weight. Besides, since only the electrode's pattern changes during the fabrication of PZT [45],

this approach does not greatly increase the expenses particularly in mass production. Except several preliminary studies regarding the traveling-wave ultrasonic motors [46], the multivibration-tailored nonuniform distribution of the ring-shaped electrodes has been rarely reported up to the present. Considering the feasibility to improve the multi-DOF PA's performance and the originality, it is meaningful to test the multivibration-tailored nonuniformly distributed electrode in PAs.

In this article, a multi-DOF self-moving PA (MDSMPA) is developed to achieve high carrying/positioning performance. Its ring-shaped electrode is nonuniformly divided into 14 portions to independently excite the fourth-order bending (B_4) and third-order bending (B_3) vibrations, which generate the translational and rotational movements, respectively, through the modulation of the frequency/voltage and the optimal arrangement of the feet. Besides, the actuator is supported by four rigid feet arranged near the outer periphery of the ring-shaped vibrating body to obtain the stability of movement. The contributions of this article locate in the following aspects.

- 1) Tailored to the vibration displacement distributions, the angle of each portion of the nonuniformly distributed electrode as well as its applied frequency/voltage are decided to balance the electromechanical coupling properties of the B_4 and B_3 vibrations. This provides a new idea to design the ring-, bar-, or even irregular-shaped actuators whose electromechanical couplings can be enhanced by dividing the electrodes tailored to multivibration modes.
- 2) The approach to determine the positions of four feet is established to permit not only the propelling/suspending functions with three feet, but also the supporting function with the other foot. This serves as a theoretical guideline for the actuators with the nonuniform electrodes as the driving feet's positions can be arranged in an optimal way.

Besides, an onboard circuit is specially designed to guarantee the untethered movement of the MDSMPA. It basically adopts the H-bridge architecture but employs an insulating module to make it applicable to the ground-shared electrodes; i.e., to the best of our knowledge, the first trial among the circuits driven by the small-sized batteries.

Benefiting from the nonuniformly distributed electrode, the MDSMPA possesses the following specifications.

- 1) The mechanical part has the size of $\Phi 50 \times 7.5$ mm³ and the weight of 32.8 g, the onboard circuit has the size of $\Phi 50 \times 40$ mm³ and the weight of 40.5 g, and the entire weight of the MDSMPA is 115.7 g.
- 2) When the MDSMPA operates in a tethered manner, it yields the maximal payload of 5130 g, equal to 156.4 times the weight of the mechanical part. Meanwhile, the translational and rotational speeds reach 156.4 mm/s and 23.5 rad/s, respectively. Besides, it crosses the 11-mm-wide gully and climbs the 10.1° slope.
- 3) In an untethered manner, the MDSMPA yields the maximal payload of 2390 g, equal to 20.7 times the entire actuator's weight. The maximal speeds are 86.5 mm/s and 15.4 rad/s for the translational and rotational movements, respectively. The minimal stepwise displacement and the

minimal stepwise angle reach 117 nm and 2.4 μ rad, respectively.

The rest of this article is organized as follows. Section II describes the configuration, operating principle, modeling, and design. Section III demonstrates the moving/carrying performance when the MDSMPA operates in a tethered manner. Section IV shows the moving/positioning performance in an untethered manner. Finally, Section V concludes this article.

II. DESIGN OF MDSMPA

A. Basic Configuration

As shown in Fig. 1(a), the kangaroo achieves the walking and rotating movements through the legs' propelling and suspending functions, and the tail's function as a supporting "leg." Inspired by this unique locomotion, three feet of the actuator have the driving function while the one foot has the supporting function. In conventional ways, to enhance the electromechanical coupling of the B_4 or B_3 vibrations, the electrodes are uniformly distributed into 8 or 6 portions, respectively [see Fig. 1(b)]. Taking the eight-portion as an example, the electromechanical coupling factors (k_{eff} , whose measuring method is given in Appendix A) are 19.1% and 8.6% for the B_4 and B_3 vibrations, respectively [see Fig. 1(c)]; this discrepancy originates from the fact that the eight-portion mismatches the region corresponding to the B_3 vibration (six-portion). Similarly, by utilizing the six equal portions, the B_4 vibration's k_{eff} (7.5%) is lower than the value of the B_3 vibration (18.3%) [see Fig. 1(d)]. Fig. 1(e) illustrates the formation of the multivibration-tailored nonuniformly distributed electrode, whose cutting lines inherit those of conventional divisions of the B_4 and B_3 vibrations. Here, the angular offset between the adjacent uniform portions is set to 7.5°, which is discussed in Section II-C. Fig. 1(f) plots the connections between the portions and the electrical ports, and the PZT plate is polarized along the z-axis. As shown in Fig. 1(g), the k_{eff} of the B_4 and B_3 vibrations are, respectively, 15.9% and 16.8%, which indicate that the nonuniformly distributed electrode balances the k_{eff} s of these two vibrations. Fig. 1(h) shows the photograph of the MDSMPA's mechanical part, composed by a PZT plate (P4H, Shenlei Corp., Shaoxing, China), a duralumin vibrating body, and four hemispheric feet. Its mechanical part weights 32.8 g.

B. Operating Principle

In terms of the movement pattern, the MDSMPA's operating principles imitate the kangaroo's locomotion to a certain extent. For both translational and rotational movements, a hindfoot (HF) with almost no deformation acts as a supporting foot, while the other feet are divided into two groups, i.e., the forefoot (FF) and the middle feet (MF), which provide the propelling and suspending functions, respectively, in an alternating way. Fig. 2(a) and (b) illustrates the operation principles of the MDSMPA's translational movement through the comparison with the walking gait of a kangaroo.

- At this stage (i), the MDSMPA and the kangaroo locate in the starting states, with all legs being passive.

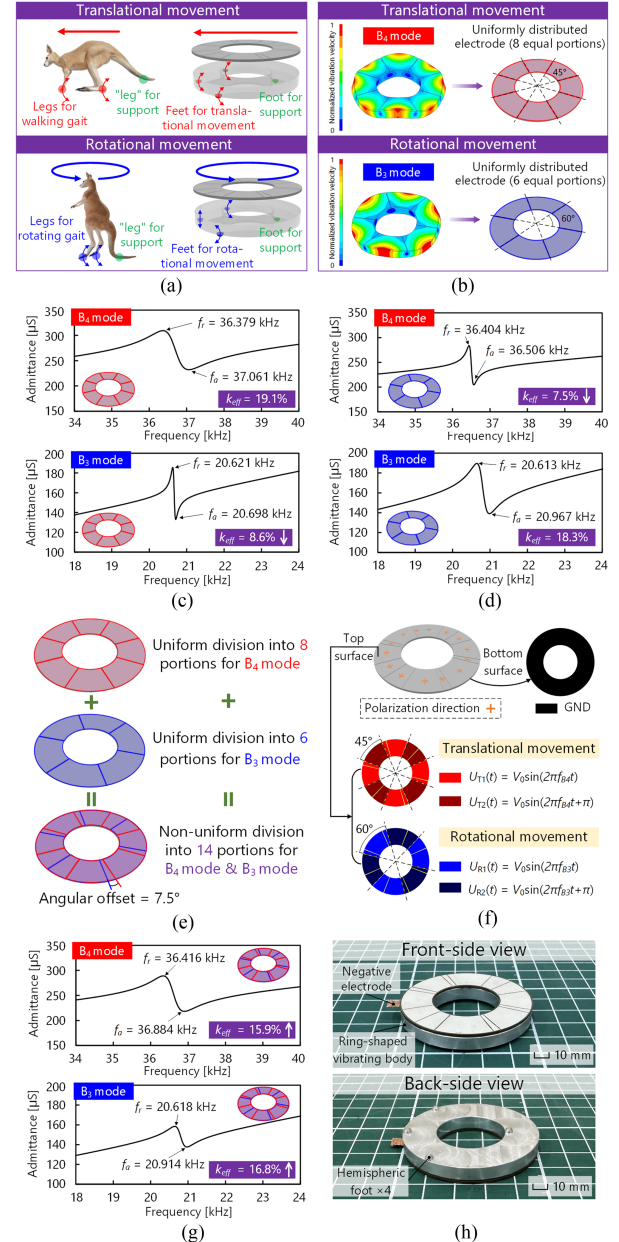


Fig. 1. Basic configuration of the MDSMPA. (a) Inspiration from the kangaroo's locomotion. (b) Conventional ways of dividing the electrode, i.e., the uniform distribution according to the vibration displacement distributions of the B_4 and B_3 modes. The admittance characteristics when the electrode is uniformly distributed into (c) 8 portions and (d) 6 portions. Here, f_r and f_a denote the resonant and anti-resonant frequencies, respectively. (e) Formation of the nonuniformly distributed electrode. (f) Connections between the electrode portions and the electrical ports. Here, V_0 means the voltage amplitude, f_{B4} and f_{B3} denote the driving frequencies corresponding to the B_4 and B_3 vibrations, respectively, and t denotes time. (g) Admittance characteristics of the MDSMPA, which adopts the nonuniformly distributed electrode. (h) Prototype.

- At the stage (ii), as shown in the side view, the MDSMPA produces the forces whose directions are tilting with the ground. The actuator's FF suspends and the MFs propel, enabling the actuator to move forward; this resembles the kangaroo's movement pattern, where the forelegs suspends and the hindlegs push against the ground.

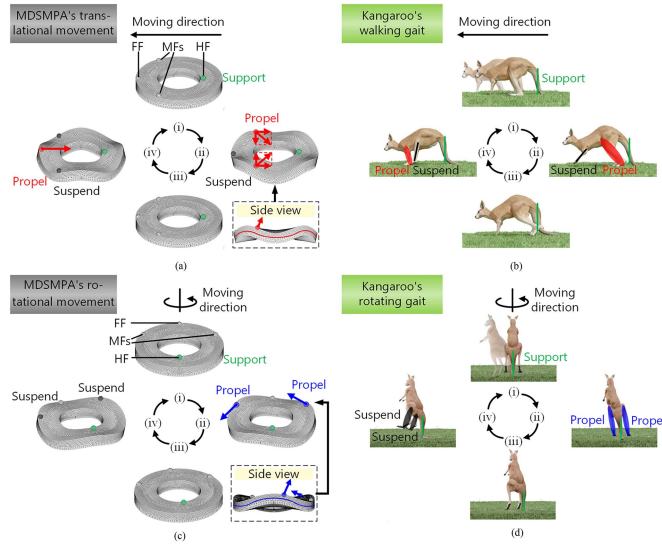


Fig. 2. MDSMPA's operating sequence. (a) Translational movement. (b) Kangaroo's walking gait. (c) Rotational movement. (d) Kangaroo's rotating gait. Here, the actuator's bottom surface is arranged upwards to illustrate the movements of the driving feet, while side-view subfigures show how the deformations of the vibrating body facilitate the driving function.

- 3) At the stage (iii), the vibration displacements of the driving feet return to zero, while all legs of the kangaroo remain passive.
- 4) At the stage (iv), the MDSMPA's FF pushes against the ground while the MFs suspend [this is opposite to the stage (ii)]; this drives the actuator to move forward. Similarly, the kangaroo alters the movements between the forelegs and hindlegs.

Fig. 2(c) and (d) shows the operation principles of the rotational movements. The similarity between the actuator's rotational movement and the kangaroo's rotating gait lies in the alternating movements of propulsion and suspension, while one leg supports the body. At the stage (i) and (iii), the MDSMPA and the kangaroo remain in the passive states. Whereas, at the stage (ii), the kangaroo's two legs propel against the ground; this is analogous to the actuator's MFs during the propulsion (see the side view in Fig. 2(a) for details). At the stage (iv), the actuator's MFs suspended; this imitates the suspension of the kangaroo's two legs. Besides, the FF's alternating propulsion and suspension movements are 180° out-of-phase with those of MFs; this strategy enhances the actuation efficiency [7].

C. Modeling and Design

1) Establish a Krimhertz-Transmission-Theory-Based Model: Fig. 3(a) shows the vibration model based on the Krimhertz transmission theory [47], [48]. The model represents the acoustic and electrical properties through series and parallel connections of several elements (e.g., impedance) [49], facilitating relatively easy assessment of the actuator's performance compared with finite element analysis [50]. Here, the foot with the supporting function is not considered as we mainly focus on the driving force. Regarding the ring-shaped

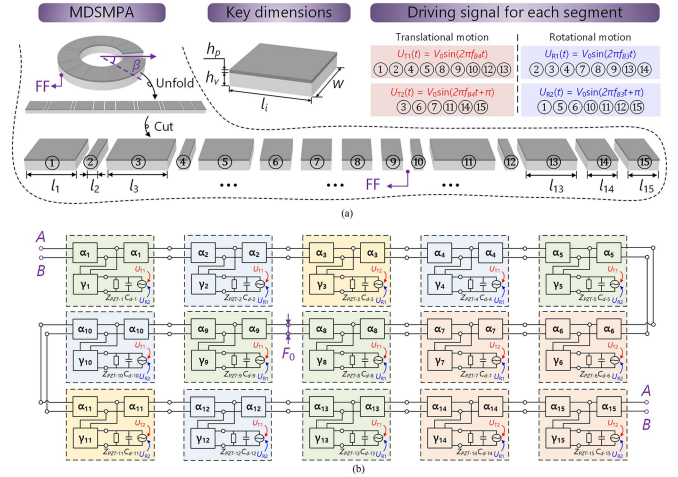


Fig. 3. Vibration model. (a) Unfolding-drawing and the division of the MDSMPA according to the electrodes' distribution and the driving foot's position. (b) Elements in the Krimhertz-transmission-theory-based model and their definitions are given in the Appendix B. Here, F_0 is the driving force.

configuration, the actuator is initially unfolded as a bar-shaped model, and subsequently divided into 15 segments according to the electrode's distribution and the position of the FF (where the driving force is produced) [36]. The length of each segment is calculated by $l_i = (D_{in}\beta_i + D_{out}\beta_i)/4$, where β_i stands for the central angle of the i th PZT segment (i is an integer), and D_{in} and D_{out} are, respectively, the inner and outer diameters of the PZT plate (and also the vibrating body). Each segment contains the power source, the impedance (Z_{PZT-i}), the clamped capacitance (C_{d-i}), two vibration-transmission elements (α_i), and the electromechanical coupling element (γ_i) [36]. Besides, α_1 's left side and α_{15} 's right side are in short connection due to the ring shape. The model is constructed in Simulink (ver. R2020a, MathWorks, Natick, USA) and analyzed through the frequency-sweeping method [7].

2) Decide the Key Dimensions of the Vibrating Body: To decide the optimal values of the vibrating body's D_{in} , D_{out} , and height (h_v), we analyze how these dimensions affect the driving-force-to-weight ratio. The driving force is calculated with the vibration model. Fig. 4(a) illustrates that, in the D_{in} range of 20–30 mm and the D_{out} range of 45–55 mm, the maximal driving-force-to-weight ratio of 0.68 exists at $(D_{in}, D_{out}) = (26, 48)$ mm. Fig. 4(b), (c), and (d) shows the variations in the driving-force-to-weight ratio against D_{in} and D_{out} when h_v equals 3, 5, and 7 mm, respectively. It is clear that the driving-force-to-weight ratio at $(D_{in}, D_{out}, h_v) = (25, 50, 5)$ mm is relatively high compared to the values corresponding to other dimensions, so they are selected for the vibrating body. The inner and outer diameters of the PZT plate are, as mentioned above, identical to those of the vibrating body; and the PZT plate's thickness (h_p) is set to 1 mm because of the commercial availability.

3) Decide the Feet's Positions:

a) FF's circumferential position: In the circumferential direction, the vibration displacement distributions of the B_3 and

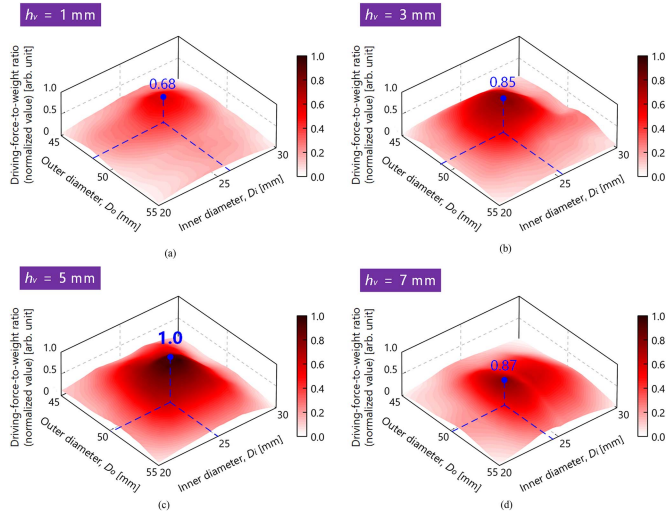


Fig. 4. Driving-force-to-weight ratio as functions of D_{in} and D_{out} at (a) $h_v = 1 \text{ mm}$, (b) $h_v = 3 \text{ mm}$, (c) $h_v = 5 \text{ mm}$, and (d) $h_v = 7 \text{ mm}$.

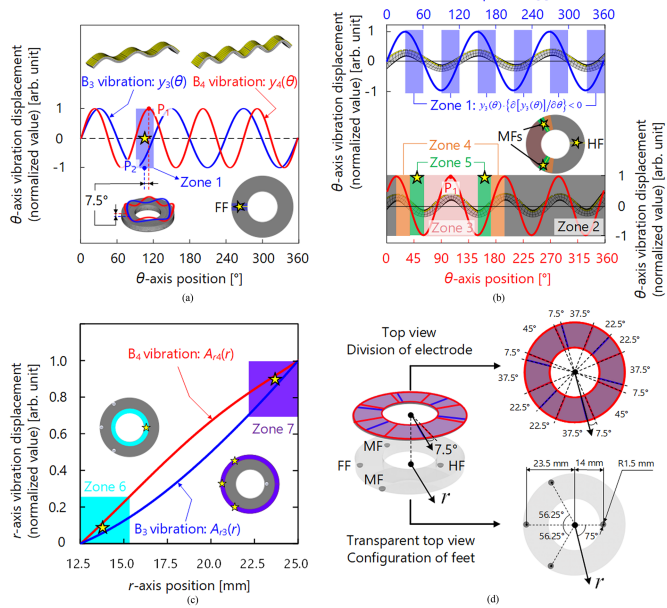


Fig. 5. Determination of the circumferential positions of (a) FF as well as (b) MFs and HF. Here, $y_3(\theta)$ and $y_4(\theta)$ are the circumferential vibration displacement distributions of the B_3 and B_4 vibrations, respectively. (c) Determination of the radial positions of FF, MFs, and HF. (d) Overall distribution of the electrode and the feet, where the specific angle corresponding to each electrode portion as well as the positions and dimensions of the feet are given.

B_4 vibrations at an instant are expressed as [31]

$$y_n(\theta) = A_v \sin(n\theta) \sin(2\pi ft) \quad (1)$$

where A_v denotes the vibration amplitude, n is circumferential wave number (4 and 3 for the B_4 and B_3 vibrations, respectively), θ is the angular position, and f means the working frequency. As shown in Fig. 5(a), to increase the vibration displacement of the FF in the translational movement, and meanwhile generate the counterclockwise rotation, the FF is arranged where the peak point of $y_4(\theta)$ (P_1) aligns with the midpoint of Zone 1 (P_2).

In this case, the angular offset [given in Fig. 1(e)] equals the phase difference (7.5°) between the B_3 and B_4 vibrations along the θ -axis.

b) Circumferential positions of MFs and HF:

Fig. 5(b) illustrates how the θ -axis positions of the MFs are decided in an excluding way. Zone 2 is initially excluded as the driving force is opposite to that produced at the FF. Besides, the counter-clockwise rotational movement exists at $y_3(\theta) \cdot \{\partial[y_3(\theta)]/\partial\theta\} < 0$ (Zone 1), allowing the exclusion of Zone 3 as a consequence of no overlap between Zone 1 and 3. Subsequently, Zone 4 is excluded owing to the negligibly small amplitude of the force component along the moving direction. Finally, the midpoints of Zone 5 are chosen as the positions of the MFs. Furthermore, to structurally balance the entire actuator, the HF is arranged 180° out of phase with the FF.

c) Radial Positions of FF, MFs, and HF:

The amplitude of the radial vibration displacement is given as [51]

$$A_r(r) = J_n\left(\alpha_n \frac{2r}{D_{out}}\right) + C_n I_n\left(\alpha_n \frac{2r}{D_{out}}\right) \quad (2)$$

where J_n is the n th order first kind of Bessel function, I_n is the n th order first kind of the modified Bessel function, α_n is the frequency constant (3.57 and 4.72, respectively, for the B_3 and B_4 vibrations) [51], r is the radial distance from the center, and C_n is the coefficient of the modified Bessel function [51]

$$C_n$$

$$= \frac{\alpha_n^2 J_n(\alpha_n) + (1-\sigma) \{ \alpha_n J_n'(\alpha_n) - n^2 J_n(\alpha_n) \}}{\alpha_n^2 I_n(\alpha_n) - (1-\sigma) \{ \alpha_n I_n'(\alpha_n) - n^2 I_n(\alpha_n) \}} \quad (3)$$

where $J_n'(\alpha_n)$ and $I_n'(\alpha_n)$ are the spatial derivatives of $J_n(\alpha_n)$ and $I_n(\alpha_n)$, respectively, and σ (0.33) represents the Poisson's ratio of duralumin. Fig. 5(c) plots the radial vibration distributions of the B_3 and B_4 vibrations, whose amplitudes are relatively high when the r -axis position approaches the edge. Since the HF acts as the supporting foot, it is arranged at the positions with small vibration displacement (Zone 6). As the FF and MFs are driving feet, they locate at the positions with large vibration displacement (Zone 7). Fig. 5(d) shows the overall distribution of the electrode and the feet. The angle between the FF and the r -axis is set to 105° and the MFs are symmetrically distributed on both sides of the FF with an angle of 56.25° . The HF locates on the opposite side of the FF. In addition, when the B_3 mode's nodal line overlaps the r axis, the angular offset between these two uniformly distributed portions is 7.5° . The distance from the FF (or MFs) to the ring's center is 23.5 mm, while the distance from the HF to the center is 14 mm. All hemispherical feet are 1.5 mm in radius. Under the excitation of two vibrations with a single PZT plate, the MDSMPA achieves both translational and rotational movements.

III. PERFORMANCE IN A TETHERED MANNER

A. Moving Performance

First, the MDSMPA's movements on a glass floor were explored when f and V_0 were varied. The voltage was applied by utilizing the power amplifiers (4052, Aigtek, Xi'an, China).

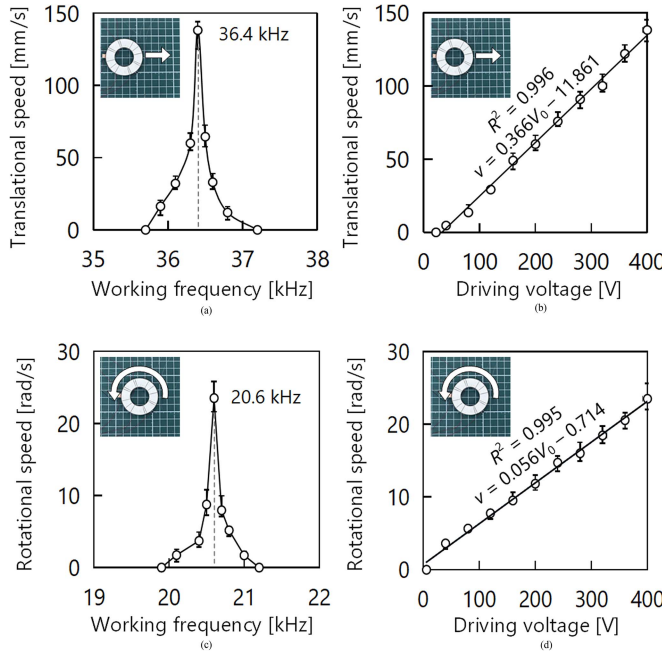


Fig. 6. Moving performance. The translational speed as functions of (a) the working frequency and (b) the driving voltage. The rotational speed as functions of (c) the working frequency and (d) the driving voltage.

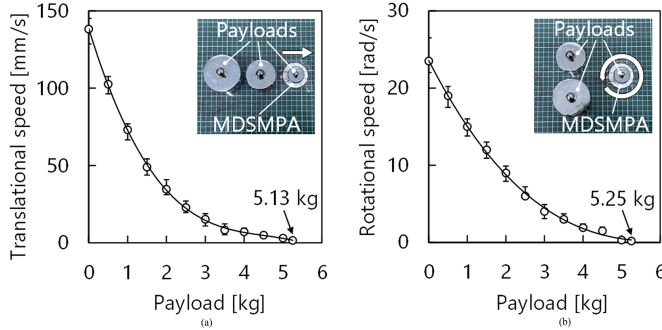


Fig. 7. Carrying performance. (a) Translational speed and (b) rotational speed as functions of the payload.

Fig. 6(a) illustrates that the translational speed has the maximal value of 138.2 mm/s at $f = 36.4$ kHz. Fig. 6(b) shows that the speed increases in a nearly linear manner with increasing V_0 . As shown in Fig. 6(c), the maximal speed corresponding to the rotational movement is 23.5 rad/s at $f = 20.6$ kHz. Fig. 6(d) shows how the rotational speed is related to V_0 ; this is similar to the relationship between the translational speed and V_0 .

B. Carrying Performance

Then, the MDSMPA's carrying performance was assessed by measuring the speed under different payloads. Here, V_0 was set to 400 V, and f was set to 36.4 and 20.6 kHz for the translational and rotational movements, respectively. Fig. 7(a) illustrates how the translational speed changes with varying payload. Observably, the speed decreased in a gradual way with increasing payload. The maximal payload reached 5130 g, equal

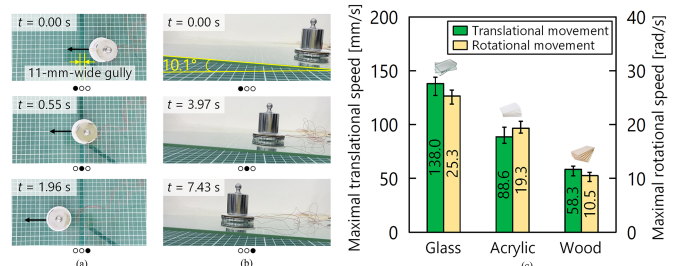


Fig. 8. MDSMPA's capability of (a) crossing the gully, (b) climbing the slope, and (c) moving on the floors made of glass, acrylic, and wood.

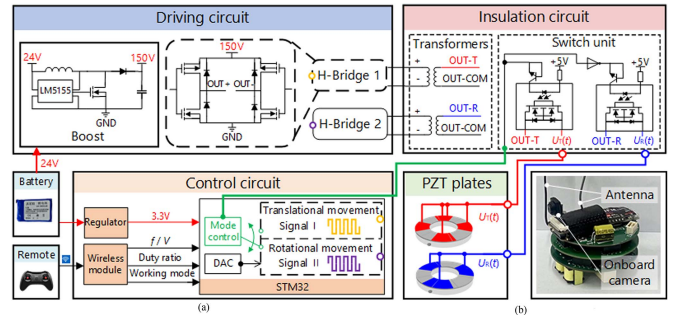


Fig. 9. Onboard circuit's (a) schematic and (b) photograph.

to 156.4 times the weight of the mechanical part (32.8 g). For the rotational movement, the maximal payload was 5250 g [see Fig. 7(b)].

C. Movements on Gully, Slope, and Different Floors

Next, the MDSMPA's movements were tested on the gully, the slope, and different floors. Fig. 8(a) illustrates that it successfully crosses a 11-mm-wide gully. Fig. 8(b) shows the actuator's capability to climb the slope of 10.1°. As shown in Fig. 8(c), the maximal speeds on the glass floor were higher than those on the floors made of acrylic and wood.

IV. PERFORMANCE IN AN UNTETHERED MANNER

A. Onboard Circuit

Initially, an onboard circuit was designed for the untethered movement. Fig. 9(a) illustrates the circuit's architecture. To reduce the size of the circuit and the consumption of the microcontroller's I/O resources, we excite half of the electrodes for both translational and rotational movement. A wireless module receives the commands from the remote controller. The microcontroller produces the signals for the driving and insulating circuits. Owing to the large clamping capacitance of the 1-mm-thick PZT plate, the amplifying circuit basically uses the H-bridge scheme. In specific, two groups of gate drivers (MASTERGAN1, STMicroelectronics, Geneva, Switzerland) are powered with a boost converter (LM5155, TI Corp., Dallas, USA). Here, the voltage is modulated by adjusting the duty ratio of the MOSFETs' gate drive signals. The voltages outputted from the H-bridge components are processed by the transformers to prevent electrical shorts as the bottom side of the PZT plate is

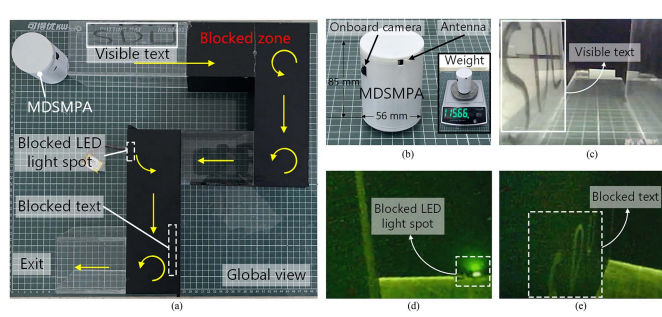


Fig. 10. Demonstration of the tube inspection. (a) Map. (b) Photograph of the untethered actuator. The images of (c) a visible text, (d) a blocked LED light spot, and (e) a blocked text. .

connected onto the duralumin vibrating body. Eight relays (G6S-2, OMRON Corp., Kyoto, Japan) switch the signals applied to one portion of the electrode. Fig. 9(b) shows the photograph of the onboard circuit, which has the size of $\Phi 50 \times 40 \text{ mm}^3$ and the weight of 40.5 g.

B. Moving/Carrying Performance

Subsequently, the MDSMPA's untethered movement was tested in continuous operation. Owing to the compact structure and the multi-DOF movements, the MDSMPA could carry out the tube inspection [see Fig. 10(a)]. As shown in Fig. 10(b), the actuator's movement is controlled with a remote controller, while a camera captures real-time images. The untethered actuator has the size of $\Phi 56 \times 85 \text{ mm}^3$ and the weight of 115.7 g. During the inspection, V_0 was set to 100 V and f followed the value in the tethered condition. As shown in Fig. 9(c), (d), and (e), The MDSMPA passed through a visible text, a blocked LED light spot, and a blocked text in sequence. Finally, it arrived the exit (see the supplementary video).

The moving/carrying performance was evaluated when the MDSMPA conducted the continuous operation. Fig. 11(a) and (b) shows that the maximal translational and rotational speeds are respectively 86.5 mm/s and 15.4 rad/s. Fig. 11(c) shows that the maximal payload corresponding to the translational movement reaches 2390 g, equal to 20.7 times the weight of entire MDSMPA. For the rotational movement, the maximal payload was 2610 g [see Fig. 11(d)].

The straightness in the translational movement and the drift in the rotational movement were assessed. Fig. 12(a) shows a series of photographs capturing the actuator's positions during the translational movement (recorded every 50 mm). Fig. 12(b) plots the actuator's central points $C_m = (x_m, y_m)$ ($m = 1\text{--}6$, where m denotes the index of the central points) at the speed of 25 mm/s. Clearly, the fitted trajectory slightly deviates from the predicted trajectory (x-axis) by 0.97°; this can be regarded as the absolute error φ [17]

$$\varphi = \arctan \frac{\sum_{m=1}^6 x_m y_m - \frac{1}{m} \left(\sum_{m=1}^6 x_m \right) \left(\sum_{m=1}^6 y_m \right)}{\sum_{m=1}^6 x_m^2 - \frac{1}{m} \left(\sum_{m=1}^6 x_m \right)^2} \quad (4)$$

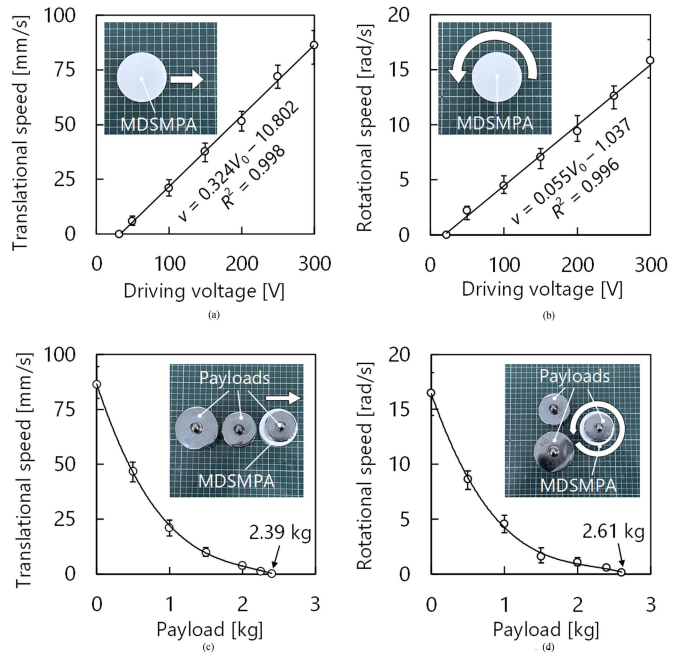


Fig. 11. Moving/carrying performance when the MDSMPA moves in an untethered manner. (a) Translational speed and (b) the rotational speed as functions of the driving voltage. (c) Translational speed and (d) the rotational speed as functions of the payload.

Besides, the relative error ranges from -4.3 to $+1.9$ mm, and the relative error band R_t is defined as

$$R_t = \max_{m=1,2,3,4,5,6} (y_m) - \min_{m=1,2,3,4,5,6} (y_m). \quad (5)$$

Fig. 12(c) illustrates that, at 75 mm/s, φ and R_t do not exceed 3.09° and 20.73 mm, respectively. As the vibrating body, the driving feet's arrangement, and the vibration mode (i.e., B_4) are symmetric [7], the actuator exhibits good linearity for the translational movement. Fig. 12(d) depicts photographs of the actuator for the rotational movement (recorded every 10°), where the actuator locates at the origin $(0, 0)$ [considered as the expected center $C_e = (x_e, y_e)$] before it starts moving. Fig. 12(e) shows the trajectories of five circles and the measured centers $C_m = (x_m, y_m)$ ($m = 1\text{--}5$). Here, the absolute error S is given as

$$S = \max_{m=1,2,3,4,5} \sqrt{(x_m - x_e)^2 + (y_m - y_e)^2} \quad (6)$$

and the relative error R_r is expressed as

$$R_r = \max_{m,m' \in \{1,2,3,4,5\}, m \neq m'} \sqrt{(x_m - x_{m'})^2 + (y_m - y_{m'})^2}. \quad (7)$$

In this case, S and R_r are calculated as 3.18 and 2.56 mm, respectively. Fig. 12(f) shows that at 15 rad/s, S and R_r do not exceed 4.15 and 3.09 mm, respectively, because the centrosymmetric vibrating body and the centrosymmetric vibration mode (i.e., B_3) decrease the drift in the rotational movement [44].

C. Positioning Performance

Followingly, the stepwise displacement/angle of the MDSMPA was measured under stepping operation. Fig. 13(a)

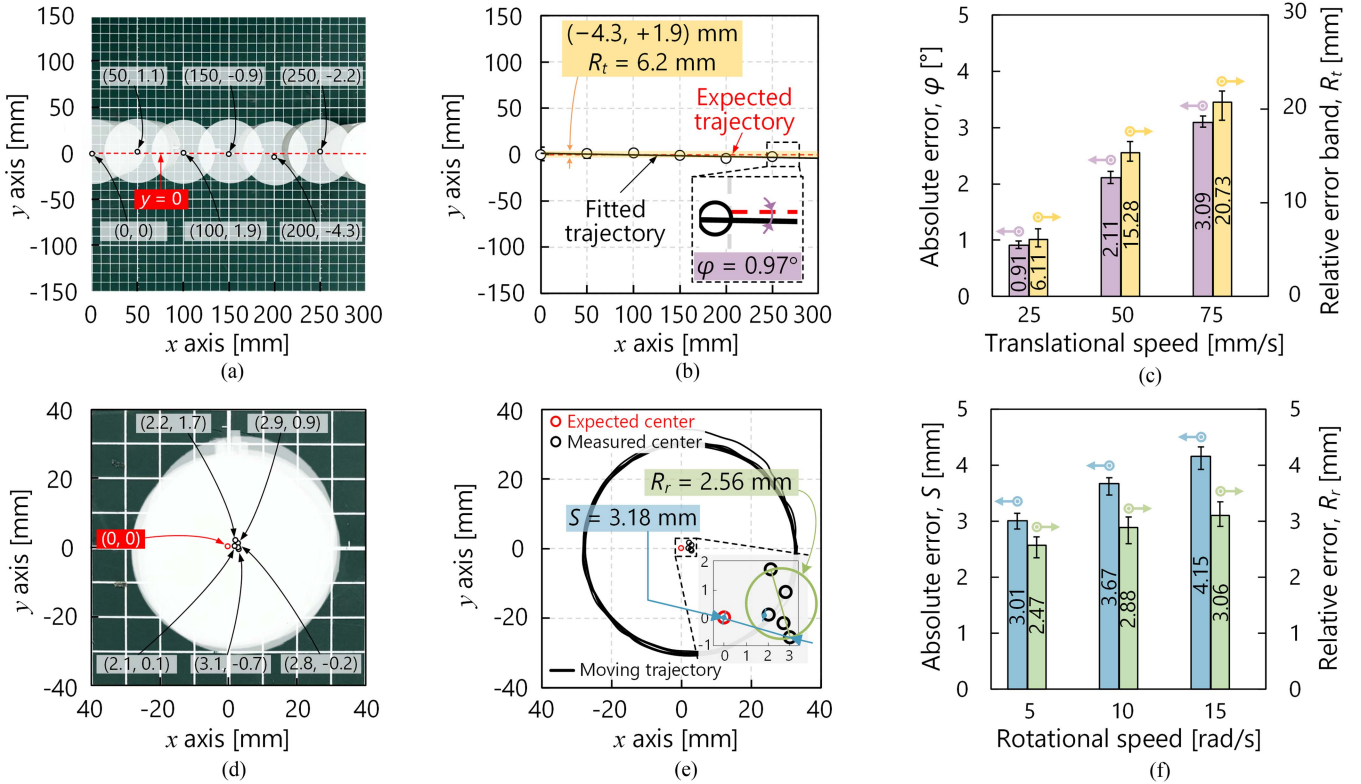


Fig. 12. Evaluation of the straightness and the drift of the MDSMPA's movement. (a) Positions. (b) Fitting line and the errors for the translational movement, and (c) the absolute errors and the relative error bands at the speeds of 25, 50, and 75 mm/s. (d) Positions. (e) Trajectory and the errors. (f) Absolute and relative errors at the speeds of 5, 10, and 15 rad/s. Here, the expected centers and trajectories are indicated as red points and dotted lines, respectively; and the measured centers and trajectories are marked by the black points and solid lines, respectively.

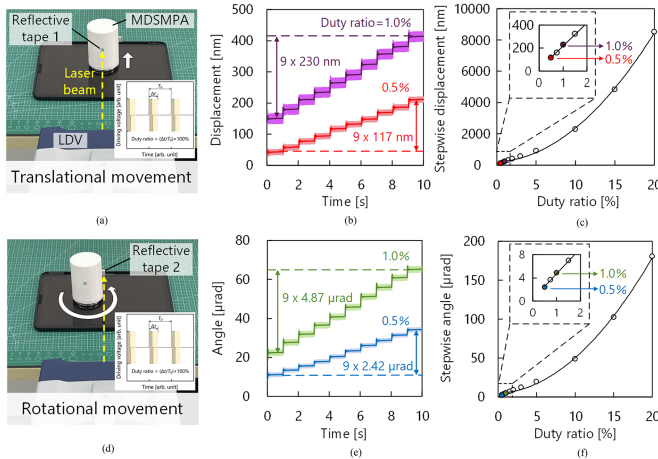


Fig. 13. Positioning performance. (a) Testbed. (b) Stepwise displacement in the time domain. (c) Stepwise displacement as a function of duty ratio for the translational movement. (d) Testbed. (e) Stepwise angle in the time domain. (f) Stepwise angle as a function of the duty ratio for the rotational movement.

illustrates the testbed, where a laser Doppler vibrometer (PSV-500, Polytec, Waldbronn, Germany) measures the stepwise displacement, and the laser beam illuminates the middle area of the MDSMPA. Here, f followed the values presented in the previous section and V_0 was set to 20 V. To adjust the voltage,

the microcontroller generates multiple signal groups with a 1 s interval (T_0) between adjacent groups, while the execution time (Δt) varies. Here, the duty ratio is defined as $(\Delta t/T_0) \times 100\%$. As shown in Fig. 13(b), the translational stepwise displacement reached 117 nm at a duty ratio of 0.5%, indicating the MDSMPA's high positioning capability. The stepwise displacement was adjusted by varying the duty ratio of the square driving waveforms. Fig. 13(c) illustrates that the stepwise displacement increases gradually as the duty ratio becomes larger. Fig. 13(d) depicts that the laser beam illuminates the edge of the MDSMPA to measure the stepwise angle. Fig. 13(e) shows that the minimal stepwise angle reaches $2.42 \mu\text{rad}$ at the duty ratio of 0.5%. Similarly, the stepwise angle exhibits the increasing tendency as the duty ratio becomes larger [see Fig. 13(f)].

D. Performance Comparison

Finally, the MDSMPA's performance was compared with those of typical PAs. The results in Table I imply the following items.

- 1) Li et al.'s [44] tripod actuator adopted the ring-shaped structure, but it only achieves the bidirectional movement as the feet's arrangement does not permit the movements in different directions though various vibration modes are provable with the ring shape. This highlights the advantage of the nonuniformly distributed electrode,

TABLE I
PERFORMANCE COMPARISON BETWEEN THE MDSMPA AND SEVERAL TYPICAL PAs

	This study	Li et al. [44]	Wang et al. [52]	Hariri et al. [35]	Wu et al. [7]
Profile	Ring-shaped quadruped	Ring-shaped tripod	Ring-shaped tripod	Rectangle-shaped quadruped	Rectangle-shaped quadruped
Size [mm ³]	Φ50 × 7.5 32.8 (tethered) 115.7 (untethered)	Φ67 × 27	20 × 20 × 4.6	180 × 60 × 0.95	54 × 52 × 46
Weight [g]		94	2.2	20.4	76.5
Operating principle	Standing wave	Standing wave	Standing/traveling waves	Traveling wave	Standing wave
DOF	3	1	3	3	3
Tethered/untethered	Tethered and untethered	Tethered	Tethered	Untethered	Untethered
Working frequency [kHz]	36.4/20.6	36.8	22.25/21.55	11.2	59.3
Maximal payload [g]	5130 (tethered) 2390 (untethered)	300	50	90	520
Payload-to-weight ratio	156.4 (tethered) 20.7 (untethered)	3.2	22.7	4.4	6.8
Maximal translational speed [mm/s]	138.2 (tethered) 86.5 (untethered)	231.6	39.3	133.3	221
Maximal rotational speed [rad/s]	23.5 (tethered) 15.4 (untethered)	-	16.5	NA	9.4
Minimal translational stepwise displacement [nm]	117 (untethered)	250	380	NA	300

which endows the flexible design (particularly the feet's arrangement) of the multi-DOF PAs.

- 2) Wang et al.'s [52] ring-shaped actuator utilized the standing and traveling waves to achieve the linear and rotational movements, respectively. However, using the separated PZT plates leads to a low k_{eff} , which dominantly causes the payload-to-weight ratio of Wang et al.'s actuator to be 0.15 times that of our MDSMPA.
- 3) Hariri et al. [35] developed an untethered actuator with three DOFs. However, since the traveling wave's intensity is easily affected by the payload, Hariri et al.'s actuator's payload is 0.038 times the value of our MDSMPA in an untethered manner. Besides, Hariri et al.'s actuator mainly uses the operational amplifiers to form the circuit, where the current and output power are relatively small compared to those of our H-bridge-based onboard circuit [53].
- 4) Wu et al.'s [7] quadruped actuator achieved high speed (221 mm/s) because it is driven with four feet, but the nonuniform movements of four feet and their phase difference inevitably weaken the controllability [11]; this causes the minimal stepwise displacement of Wu et al.'s actuator to be 2.6 times the value of our MDSMPA. Moreover, under untethered operation, the payload-to-weight ratio of Wu et al.'s actuator is 0.33 times the value of our MDSMPA; this should originate from the improvement in electromechanical coupling properties [54], induced by the non-uniformly distributed electrode.

V. CONCLUSION

This article presented the proposal, design, and performance evaluation of the MDSMPA with the vibration-tailored non-uniformly distributed electrode. Through numerical analysis and experimental investigation, we have drawn the following conclusions.

- 1) To balance the electromechanical coupling factors between the B_4 and B_3 vibrations, we developed a ring-shaped electrode with nonuniform distribution,

which was applied to the MDSMPA to generate the multi-DOF movements.

- 2) The optimal positions to arrange the feet were decided to permit the supporting function with one foot as well as the propelling/suspending functions with the other feet.
- 3) A Krimhertz-transmission-theory-based model was built to enhance the driving-force-to-weight ratio of the MDSMPA.
- 4) In a tethered manner, the MDSMPA had the maximal speed of 138.2 mm/s and the maximal payload of 5130 g. Besides, the MDSMPA crossed the 11-mm-wide gully, climbed the slope of 10.1°, and moved on the floors made of glass, acrylic, and wood.
- 5) In an untethered manner, the MDSMPA yielded the minimal stepwise displacement of 117 nm and the minimal stepwise angle of 2.4 μrad. Moreover, it carried out the tube inspection, which benefits from the multi-DOF untethered movement.

The conclusions not only show the effectiveness of our proposal but offer a new approach for designing the multi-DOF PAs. In the future, we attempt to coordinate other vibration modes with various types of nonuniformly distributed electrodes. The design philosophy of the onboard circuit with more channels also deserves further investigation.

APPENDIX

A. Method to Measure Electromechanical Coupling Factors

The k_{eff} s were measured by using the following procedures, where the vibration mode B_3 was chosen as an example [see Fig. 1(g)].

- 1) Use an impedance analyzer (ZX70AX, Zhixin Precision Electronics, Changzhou, China) [see Fig. 14(a)] to measure the admittance curve.
- 2) Focus on the zone corresponding to a certain vibration mode. Fig. 14(b) illustrates the theoretical results.

$$\alpha_i =$$

$$\begin{aligned} & \left[\cos \left\{ (2\pi f_{Bq})^{\frac{1}{2}} \cdot \frac{l_i}{2} \cdot \left[\frac{12(\rho_p h_p w + \rho_{AL} h_v w)}{(c_{11} h_p w + E_{AL} h_v w)(h_p + h_v)^2} \right]^{\frac{1}{4}} \right\} \right. \\ & \left. - j \sin \left\{ (2\pi f_{Bq})^{\frac{1}{2}} \cdot \frac{l_i}{2} \cdot \left[\frac{12(\rho_p h_p w + \rho_{AL} h_v w)}{(c_{11} h_p w + E_{AL} h_v w)(h_p + h_v)^2} \right]^{\frac{1}{4}} \right\} \right] \\ & \left[(2\pi f_{Bq})^{\frac{1}{2}} \left[\frac{1}{12} (c_{11} h_p w + E_{AL} h_v w) (h_p + h_v)^2 (\rho_p h_p w + \rho_{AL} h_v w) \right]^{\frac{1}{4}} \right] \\ & \times \sin \left\{ (2\pi f_{Bq})^{\frac{1}{2}} \cdot \frac{l_i}{2} \cdot \left[\frac{12(\rho_p h_p w + \rho_{AL} h_v w)}{(c_{11} h_p w + E_{AL} h_v w)(h_p + h_v)^2} \right]^{\frac{1}{4}} \right\} \\ & \cos \left\{ (2\pi f_{Bq})^{\frac{1}{2}} \cdot \frac{l_i}{2} \cdot \left[\frac{12(\rho_p h_p w + \rho_{AL} h_v w)}{(c_{11} h_p w + E_{AL} h_v w)(h_p + h_v)^2} \right]^{\frac{1}{4}} \right\} \end{aligned} \quad (A2)$$

$$(i = 1 - 15; q = 3, 4)$$

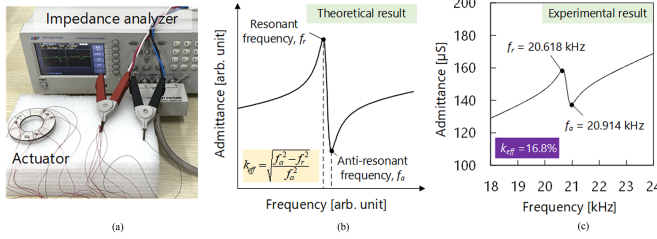


Fig. 14. Measurement of the k_{eff} s. (a) Testbed. (b) Theoretical result. (c) Experimental result.

3) Calculate the k_{eff} with the following equation:

$$k_{eff} = \sqrt{\frac{f_a^2 - f_r^2}{f_a^2}}. \quad (A1)$$

As shown in Fig. 14(c), $f_r = 20.618$ kHz and $f_a = 20.914$ kHz. Therefore, k_{eff} equals 16.8%. Other k_{eff} s were obtained with the same procedures, despite the differences in the electrode division method and the excitation zone.

B. Definitions of Elements in Model

The elements given in Fig. 3(b) are defined according to the actuator's configuration, dimensions, and material constants. First, the vibration-transmission element α_i is given as [47]. (A2) shown at the top of this page where j is the imaginary unit, $w = (D_{out} - D_{in})/2$ is the width of the ring; ρ_p (7.8×10^3 kg/m³) and ρ_{AL} (2.7×10^3 kg/m³) are, respectively, the densities of the PZT plate and the duralumin vibrating body, c_{11} (145 GPa) is the Young's modulus of the PZT plate orthogonal to the polarization direction, and E_{AL} (70.3 GPa) is the Young's modulus of duralumin. In addition, the electromechanical coupling element γ_i is given as [36]

$$\gamma_i = \begin{bmatrix} 0 & \frac{j h_p \rho_p^{\frac{1}{2}} c_{11}^{-\frac{1}{2}}}{2e_{31} \sin(\pi l_i f_{Bq} \rho_p^{\frac{1}{2}} c_{11}^{-\frac{1}{2}})} \\ \frac{2j e_{31} \sin(\pi l_i f_{Bq} \rho_p^{\frac{1}{2}} c_{11}^{-\frac{1}{2}})}{h_p \rho_p^{\frac{1}{2}} c_{11}^{-\frac{1}{2}}} & 0 \end{bmatrix} \quad (A3)$$

$$(i = 1 - 15; q = 3, 4)$$

where e_{31} (6.8 C/m²) denotes the piezoelectric constant [15]. Z_{PZT-i} and C_{d-i} are, respectively, expressed as [51]

$$Z_{PZT-i} = \frac{w}{h_p} \cdot e_{31}^2 \rho_p^{-\frac{1}{2}} c_{11}^{-\frac{1}{2}} \cdot \sin \left(l_i \cdot 2\pi f_{Bq} \rho_p^{\frac{1}{2}} c_{11}^{-\frac{1}{2}} \right) \quad (i = 1 - 15; q = 3, 4) \quad (A4)$$

and

$$C_{d-i} = \frac{\varepsilon_{33} S l_i w}{h_p} \quad (i = 1 - 15) \quad (A5)$$

where ε_{33} is the dielectric constant (13.01×10^{-9} F/m) [15].

REFERENCES

- [1] J. Li, H. Huang, and H. Zhao, "A piezoelectric-driven linear actuator by means of coupling motion," *IEEE Trans. Ind. Electron.*, vol. 65, no. 3, pp. 2458–2466, Mar. 2018.
- [2] B. Hao, L. Wang, R. Wang, Y. Sun, J. Jin, and Q. Xu, "Numerical analysis and experimental investigation on a novel piezoelectric-actuated rail-type mobile platform," *IEEE/ASME Trans. Mechatron.*, vol. 27, no. 2, pp. 744–752, Apr. 2022.
- [3] X. Zhou et al., "A 7 cm-scale spherical underwater robot using piezoelectric double-jet actuator for deep-sea environment," *IEEE/ASME Trans. Mechatron.*, vol. 29, no. 5, pp. 3277–3288, Dec. 2023.
- [4] H. Jin et al., "Review on piezoelectric actuators based on high-performance piezoelectric materials," *IEEE Trans. Ultrasonics, Ferroelect., Freq. Control*, vol. 69, no. 11, pp. 3057–3069, Nov. 2022.
- [5] X. Li, Z. Xu, W. Sun, and H. Huang, "An auxiliary friction method for miniaturizing the inertial impact piezoelectric actuators," *IEEE Trans. Ind. Electron.*, vol. 71, no. 1, pp. 777–787, Jan. 2024.
- [6] R. Wang, L. Wang, B. Jia, J. Jin, and D. Wu, "Semi-analytical modeling and experimental evaluation on a novel standing wave rotary piezoelectric actuator driven by single-phase signal," *Mech. Syst. Signal Process.*, vol. 163, Jan. 2022, Art. no. 108177.
- [7] J. Wu et al., "Development of an untethered ultrasonic robot with fast and load-carriable movement imitating rotatory galloping gait," *IEEE/ASME Trans. Mechatron.*, vol. 30, no. 2, pp. 1001–1013, Apr. 2025, doi: 10.1109/TMECH.2024.3409574.
- [8] Y. Zhu et al., "A piezoelectric unimorph actuator-based tip-tilt-piston micromirror with high fill factor and small tilt and lateral shift," *Sens. Actuator A Phys.*, vol. 167, no. 2, pp. 495–501, Jun. 2011.
- [9] J. Deng, Z. Liu, J. Li, S. Zhang, and Y. Liu, "Development of a highly adaptive miniature piezoelectric robot inspired by earthworms," *Adv. Sci.*, vol. 11, no. 29, Jun. 2024, Art. no. 2403426.
- [10] S. Rios, A. Fleming, and Y. Yong, "Miniature resonant ambulatory robot," *IEEE Robot. Autom. Lett.*, vol. 2, no. 1, pp. 337–343, Jan. 2017.
- [11] L. Wang, W. Chen, J. Liu, J. Deng, and Y. Liu, "A review of recent studies on non-resonant piezoelectric actuators," *Mech. Syst. Signal Process.*, vol. 133, Nov. 2019, Art. no. 106254.
- [12] K. Rao, M. Hamza, P. Kumar, and K. Sravani, "Design and optimization of MEMS based piezoelectric actuator for drug delivery systems," *Microsyst. Technol.*, vol. 26, no. 5, pp. 1671–1679, May 2020.

- [13] L. Clark, B. Shirinzadeh, U. Bhagat, J. Smith, and Y. Zhong, "Development and control of a two DOF linear-angular precision positioning stage," *Mechatronics*, vol. 32, pp. 34–43, Dec. 2015.
- [14] N. Jafferis and R. Wood, "The delta-motor: A multi-modal, high-speed, flexure-based piezoelectric motor," *Sens. Actuators A Phys.*, vol. 366, Feb. 2024, Art. no. 114927.
- [15] J. Liu et al., "A self-moving piezoelectric actuator with high carrying/positioning capability via bending-resonant-vibration-induced stick-slip motion," *IEEE Trans. Ind. Electron.*, vol. 72, no. 2, pp. 1829–1839, Feb. 2025.
- [16] S. Wang et al., "Design and driving characteristics of a novel 'pusher' type piezoelectric actuator," *Smart Mater. Struct.*, vol. 25, no. 1, Nov. 2015, Art. no. 015005.
- [17] Y. Li and Q. Xu, "A novel piezo-actuated XY stage with parallel, decoupled, and stacked flexure structure for micro-/nano-positioning," *IEEE Trans. Ind. Electron.*, vol. 58, no. 8, pp. 3601–3615, Aug. 2011.
- [18] S. Zhang et al., "Piezo robotic hand for motion manipulation from micro to macro," *Nature Commun.*, vol. 14, no. 1, Jan. 2023, Art. no. 500.
- [19] J. Li et al., "A bionic type piezoelectric actuator based on walking motion and asymmetrical L-shaped flexure mechanisms," *IEEE/ASME Trans. Mechatron.*, vol. 28, no. 3, pp. 1326–1336, Jun. 2023.
- [20] L. Yan et al., "A dual-mode stick-slip piezoelectric actuator imitating mantis forefoot," *Int. J. Mech. Sci.*, vol. 266, Mar. 2024, Art. no. 108985.
- [21] T. Wang et al., "Design of a flexure-based parallel XY micro-positioning stage with millimeter workspace and high bandwidth," *Sens. Actuators A Phys.*, vol. 331, Nov. 2021, Art. no. 112899.
- [22] H. Huang, L. You, Y. Wu, Z. Xu, and X. Li, "Achieving stable and effective stick-slip motions of piezoelectric actuators with a small mass rotor by means of the auxiliary friction," *IEEE Trans. Ind. Electron.*, vol. 71, no. 10, pp. 12835–12845, Oct. 2024.
- [23] T. Cheng, M. He, H. Li, X. Lu, H. Zhao, and H. Gao, "A novel trapezoid-type stick-slip piezoelectric linear actuator using right circular flexure hinge mechanism," *IEEE Trans. Ind. Electron.*, vol. 64, no. 7, pp. 5545–5552, Jul. 2017.
- [24] J. Tang, H. Fan, J. Liu, and H. Huang, "Suppressing the backward motion of a stick-slip piezoelectric actuator by means of the sequential control method (SCM)," *Mech. Syst. Signal Process.*, vol. 143, Sep. 2020, Art. no. 106855.
- [25] G. Qiao, P. Ning, X. Xia, Y. Yu, X. Lu, and T. Cheng, "Achieving smooth motion for piezoelectric stick-slip actuator with the inertial block structure," *IEEE Trans. Ind. Electron.*, vol. 69, no. 4, pp. 3948–3958, Apr. 2022.
- [26] P. Tenzer and R. Mrad, "A systematic procedure for the design of piezoelectric inchworm precision positioners," *IEEE/ASME Trans. Mechatron.*, vol. 9, no. 2, pp. 427–435, Jun. 2004.
- [27] J. Deng et al., "Development and experiment evaluation of a compact inchworm piezoelectric actuator using three-jaw type clamping mechanism," *Smart Mater. Struct.*, vol. 31, no. 4, Mar. 2022, Art. no. 045020.
- [28] S. Salisbury, D. Waechter, R. Mrad, S. Prasad, R. Blacow, and B. Yan, "Design considerations for complementary inchworm actuators," *IEEE/ASME Trans. Mechatron.*, vol. 11, no. 3, pp. 265–272, Jun. 2006.
- [29] Q. Lu, J. Ma, X. Lin, Y. Hu, J. Li, and J. Wen, "The development of piezoelectric inchworm actuator clamped with magnetorheological elastomer and its potential application in brain-computer interface implantation," *IEEE Trans. Ind. Electron.*, vol. 70, no. 4, pp. 4018–4026, Apr. 2023.
- [30] Z. Li, R. Zhu, X. Yi, and S. Dong, "A high-power-density piezoelectric actuator operating in bicycling movement mechanism," *IEEE Trans. Ind. Electron.*, vol. 70, no. 6, pp. 6090–6098, Jun. 2023.
- [31] J. Wu, Y. Mizuno, and K. Nakamura, "A rotary motor operating in torsional/bending modes with high torque density and high power density," *IEEE Trans. Ind. Electron.*, vol. 68, no. 7, pp. 6109–6120, Jul. 2021.
- [32] J. Wu et al., "Development of a self-moving ultrasonic actuator with high carrying/towing capability driven by longitudinal traveling wave," *IEEE/ASME Trans. Mechatron.*, vol. 28, no. 1, pp. 267–279, Feb. 2023.
- [33] S. Wang et al., "A survey of piezoelectric actuators with long working stroke in recent years: Classifications, principles, connections and distinctions," *Mech. Syst. Signal Process.*, vol. 123, pp. 591–605, May 2019.
- [34] J. Liu, J. Wu, X. Gao, Z. Ding, and W. Wei, "Enhancement of torque density and power density of polymer-based ultrasonic motors via flexible usage of anisotropy in elastic property," *Smart Mater. Struct.*, vol. 32, no. 7, Jun. 2023, Art. no. 075020.
- [35] H. Hariri, Y. Bernard, and A. Razek, "2-D traveling wave driven piezoelectric plate robot for planar motion," *IEEE/ASME Trans. Mechatron.*, vol. 23, no. 1, pp. 242–251, Feb. 2018.
- [36] L. Wang et al., "A millipede-inspired miniature ultrasonic actuator with high carrying capability and nanometer resolution," *Int. J. Mech. Sci.*, vol. 267, Apr. 2024, Art. no. 109017.
- [37] X. Tian, Y. Liu, J. Deng, L. Wang, and W. Chen, "A review on piezoelectric ultrasonic motors for the past decade: Classification, operating principle, performance, and future work perspectives," *Sens. Actuators A Phys.*, vol. 306, May 2020, Art. no. 111971.
- [38] A. Baisch, O. Ozcan, B. Goldberg, D. Ithier, and R. Wood, "High speed locomotion for a quadrupedal microrobot," *Int. J. Robot. Res.*, vol. 33, no. 8, pp. 1063–1082, Jul. 2014.
- [39] A. Dharmawan, H. Hariri, S. Foong, G. Soh, and K. Wood, "Steerable miniature legged robot driven by a single piezoelectric bending unimorph actuator," in *Proc. IEEE Int. Conf. Robot. Automat.*, Singapore, 2017, pp. 6008–6013.
- [40] G. Warburton, "The vibration of rectangular plates," *Proc. Inst. Mech. Engineers C-J. Mech.*, vol. 168, pp. 371–384, Jan. 1954.
- [41] K. Takemura and T. Maeno, "Design and control of an ultrasonic motor capable of generating multi-DOF motion," *IEEE/ASME Trans. Mechatron.*, vol. 6, no. 4, pp. 499–506, Aug. 2001.
- [42] Y. Zhao, S. Zhang, J. Deng, J. Li, and Y. Liu, "Development of a 3-DOF planar monopod piezoelectric robot actuated by multidirectional spatial elliptical trajectories," *IEEE Trans. Ind. Electron.*, vol. 71, no. 11, pp. 14673–14682, Nov. 2024.
- [43] J. Li, J. Deng, S. Zhang, and Y. Liu, "Development of a miniature quadruped piezoelectric robot combining fast speed and nano-resolution," *Int. J. Mech. Sci.*, vol. 250, Jul. 2023, Art. no. 108276.
- [44] J. Li, J. Deng, Y. Liu, S. Zhang, and K. Li, "Development of a planar tripodal piezoelectric robot with a compact ring structure," *IEEE/ASME Trans. Mechatron.*, vol. 27, no. 5, pp. 3908–3919, Oct. 2022.
- [45] Z. Li, B. Dong, and D. Zhang, "Influence of polarization on properties of 0–3 cement-based PZT composites," *Cement Concrete Comp.*, vol. 27, no. 1, pp. 27–32, Jan. 2005.
- [46] H. Hirata and S. Ueha, "Design of a traveling wave type ultrasonic motor," *IEEE Trans. Ultrasonics, Ferroelect., Freq. Control*, vol. 42, no. 2, pp. 225–231, Mar. 1995.
- [47] R. Krimholtz, D. Leedom, and G. Mattheai, "New equivalent circuits for elementary piezoelectric transducers," *Electron. Lett.*, vol. 6, no. 13, pp. 398–399, Jun. 1970.
- [48] C. Desilets, J. Fraser, and G. Kino, "The design of efficient broad-band piezoelectric transducers," *IEEE Trans. Sonics Ultrasonics*, vol. 25, no. 3, pp. 115–125, May 1978.
- [49] D. Leedom, R. Krimholtz, and G. Mattheai, "Equivalent circuits for transducers having arbitrary even- or odd-symmetry piezoelectric excitation," *IEEE Trans. Sonics Ultrasonics*, vol. 18, no. 3, pp. 128–141, Jul. 1971.
- [50] H. Kwun, W. Jolly, G. Light, and E. Wheeler, "Effects of variations in design parameters of ultrasonic transducers on performance characteristics," *Ultrasonics*, vol. 26, no. 2, pp. 65–72, Mar. 1988.
- [51] S. Ueha and Y. Tomikawa, "Rotary motors. Part 1: Disk-or ring-type motors," in *Ultrasonic Motors: Theory and Applications*. New York, NY, USA: Oxford Univ. Press, 1993.
- [52] W. Wang, J. Deng, J. Li, S. Zhang, and Y. Liu, "A small and agile ring-shaped tripodal piezoelectric robot driven by standing and traveling mechanical waves," *IEEE Trans. Ind. Electron.*, vol. 71, no. 3, pp. 2769–2778, Mar. 2024.
- [53] X. Wang, J. Liu, S. Ouyang, T. Xu, F. Meng, and S. Song, "Control and experiment of an H-bridge-based three-phase three-stage modular power electronic transformer," *IEEE Trans. Power Electron.*, vol. 31, no. 3, pp. 2002–2011, Mar. 2016.
- [54] J. Wu, Y. Mizuno, and K. Nakamura, "Polymer-based ultrasonic motors utilizing high-order vibration modes," *IEEE/ASME Trans. Mechatron.*, vol. 23, no. 2, pp. 788–799, Jan. 2018.



Jinshuo Liu was born in Shandong, China, in 2001. He received the bachelor's degree in automation in 2024 from Shandong University, Jinan, China, where he is currently working toward the master's degree in control science and engineering.

His research interests include piezoelectric actuation and its application to precise manipulation/operation.



Zhaochun Ding was born in Shandong, China, in 2001. He received the bachelor's degree in mechanical engineering in 2023 from Shandong University, Jinan, China, where he is currently working toward the master's degree in control science and engineering.

His research interests include piezoelectric actuation and its application to miniature robots.



Xuewen Rong received the B.S. and M.S. degrees in control science and engineering from Shandong University of Science and Technology, Qingdao, China, in 1996 and 1999, respectively, and the Dr. Eng. degree from Shandong University, Jinan, China, in 2013.

He is currently a Professor with School of Control Science and Engineering, Shandong University. His research interests include bionic robotics, mechatronics, and control systems.



Zihan Zhu was born in Shandong, China, in 2003. She is currently working toward the Undergraduate degree in robotics engineering with the School of Electrical and Automation Engineering, Shandong University of Science and Technology, Qingdao, China.

Her research interests include piezoelectric actuation and control system.



Rui Song received the B.S. degree in industrial automation and the M.S. degree in control theory and engineering from Shandong University of Science and Technology, Jinan, China, in 1998 and 2001, respectively, and the Dr. Eng. degree in control theory and engineering from Shandong University, Jinan, in 2011.

He is currently a Professor with School of Control Science and Engineering, Shandong University. His research interests include intelligent bionic robots, control theory and application, and automation engineering.



Jiang Wu was born in Liaoning, China, in 1988. He received the B.E. degree in mechanical engineering from Dalian University of Technology, Dalian, China, in 2010, the M.E. degree in mechatronic engineering from the State Key Laboratory of Robotics and System, Harbin Institute of Technology, Harbin, China, in 2012, and the Dr. Eng. degree in electric and electronic engineering from the Future Interdisciplinary Research of Science and Technology, Tokyo Institute of Technology, Yokohama, Japan, in 2017.

He is currently a Professor with the School of Control Science and Engineering, Shandong University, Jinan, China, where he is active in developing ultrasonically levitating devices and piezoelectric actuators/robots.



Yibin Li received the B.S. degree in automation engineering from Tianjin University, Tianjin, China, in 1982, the M.S. degree in electrical engineering from Shandong University of Science and Technology, Jinan, China, in 1990, and the Dr. Eng. degree in automation engineering from Tianjin University, in 2008.

He is currently a Professor with School of Control Science and Engineering, Shandong University, Jinan, China. His research interests include intelligent robots, special robots, intelligent vehicles, intelligent control, and mechatronics.